
Article:
MacInnes, J.M. and Zambri, M.K.S. (2015) Hydrodynamic characteristics of a rotating spiral fluid-phase contactor. Chemical Engineering Science, 126. pp. 427-439. ISSN 0009-2509

https://doi.org/10.1016/j.ces.2014.12.036

Hydrodynamic Characteristics of a Rotating Spiral Fluid-Phase Contactor

Jordan M. MacInnes* and Mohamed K. S. Zambri

* Corresponding author

Chemical and Biological Engineering

University of Sheffield

Mappin Street

Sheffield, S1 3JD, UK

Tel. +44 114 222 7511

Fax. +44 114 222 7501

Email j.m.macinnes@sheffield.ac.uk

Hydrodynamic Characteristics of a Rotating Spiral Fluid-Phase Contactor

Jordan M. MacInnes and Mohamed K. S. Zambri

Summary

Rotating spiral channels enable any two immiscible fluid phases to flow counter-currently in parallel layers allowing independent control of phase flow rates and layer thicknesses. This opens the possibility of application over the full range of fluid contacting operations, including distillation, absorption, extraction and multiphase reaction with separation. A device has been developed that enables wide-ranging experimental studies to support model refinement and design of first-generation applied devices. In this first work with the new device hydrodynamic characteristics are studied for gas-liquid systems as functions of phase flow rates, rotation rate and liquid viscosity. Measurement of the heavy phase layer thickness, using image analysis based on the Young-Laplace theory for interface shape, and measurement of volume flow rate of each phase and pressure and temperature in the spiral channel allows rigorous comparisons with an existing 'wide-channel' model relating flow rates and layer thicknesses to phase properties, geometry and rotation rate. The measured thickness of the heavy-phase layer is predicted well by the wide-channel model at high rotation and phase flow rates, where the deviation from a uniform layer thickness due to menisci at the channel end walls and interface tilt from gravity are small. At low rotation rates, where significant meniscus height and tilt develop, the layer thickness is over-predicted by the wide channel model. The sub 20 µm heavy-phase layer thicknesses measured suggest operation at optimum thickness is possible with the rotating spiral over a wide range of phase and solute systems.

Key words: rotation; spiral channel; counter-current fluid flow; multiphase; interface

1 Introduction

The use of rotating spiral channels to produce counter-current flow of immiscible fluid phases opens up new possibilities for separation and reaction operations. This approach avoids mixing of the phases so the effects of interfacial properties become secondary and the simultaneous and independent control of relative flow rates and relative element sizes of the phases is possible. MacInnes et al. (2010) demonstrated the approach experimentally by application to a binary distillation. Heating was used to generate the vapour flow with the fluids remaining confined to the rotating unit. The theory of flow and mass transfer was then developed in MacInnes et al. (2012) for a dilute solute transferring in the flow of two Newtonian phases in an infinitely wide channel with negligible gravity effect.

Use of a rotating spiral channel is mentioned in a series of patents from the 1930s (Podbielniak, 1935, 1936, 1937 and 1938) in which advantages of using centrifugal force in counter-current operations for both gas-liquid and liquid-liquid contacting are described. During World War II liquid-liquid devices were used in the production of penicillin (Anderson and Lau, 1955; Podbielniak et al., 1970), although these devices used concentric

perforated cylindrical shells as packing, rather than spiral channels. A series of papers appeared in the 1950s and 1960s (including Barson and Beyer, 1953; Jacobsen and Beyer, 1956; Kaiser, 1955; Todd and Podbielniak, 1965) using the perforated packing and reaching centrifugal acceleration up to 1000g. The only mention of the spiral channel is in the discussion at the end of the Barson and Beyer paper in which Podbielniak comments that perforated cylindrical shells "seem to work much better" than the spiral channel. So a rotating spiral was evidently tested but no results seem to have been published.

Why the rotating spiral idea was dropped is not clear, but the horizontal orientation of the rotation axis in all of the designs is clearly a problem. While the level of centrifugal acceleration is large compared to gravity, the component along a spiral channel is relatively small. Thus, gravity adds to centrifugal driving force at some positions along the channel but subtracts from it at others, producing variable phase layer thicknesses and potentially preventing control of the phase layers altogether. This along with large channel size means typical operation was in the regime of unstable interface and flow (MacInnes et al., 2012). A further difficulty in the designs is that the inlets and outlets remained unsegregated, with phase intermixing resulting in the usual problems of distribution and separation of the phases at each end of the device. This early work demonstrates the advantages of using centrifugal force for fluid-fluid contacting operations. Kaiser (1955) shows a photograph of a Podbielniak centrifugal extractor that is dwarfed by the conventional packed column it has replaced. The small size of the centrifugal unit allows expensive corrosion resistant materials and coatings to be used economically, reduces fluid inventory, means all maintenance operations are at ground level and, of course, decreases plant size. Further, as pointed out in the paper, developing a design is convenient since a thin representative slice of the final rotating unit can be tested first with the full scale throughput achieved simply by increasing the width in the axial direction. (Results for a single spiral channel tested here, for example, can scale reliably to larger throughput by stacking a number of channels.)

Subsequent work on rotating packed beds progressed independently of this earlier work. Vivian et al. (1965) operated a gimbal-mounted packed bed column at the end of the 35 ft. rotating arm of an M.I.T. instrument test centrifuge. The relatively modest 7g centrifugal acceleration used was intended to test the effect of gravity as represented in existing mass transfer correlations. Ramshaw and Mallinson (1981) initiated the use of random packing in a vertical-axis device, typically applied to gas-liquid contacting. A large number of papers have followed, principally exploring a range of applications, testing different packing geometry, attempting to visualise the resulting two phase flow in the packing and determining mass transfer performance experimentally. The papers are reviewed by Rao et al. (2004), Zhao et al. (2010) and in Visscher et al. (2013).

A further area of work employing centrifugal acceleration for fluid-phase contacting uses rotating conical or disc surfaces, often interleaved with static conical or disc surfaces (Buhtz, 1927; Huffman and Urey, 1937; Strand et al., 1962; Bruin, 1969; Wood and Watts, 1973; Makarytchev et al., 1998, 2001; Burns et al. 2003; and briefly reviewed in Visscher et al., 2013). The key difference in relation to the rotating packed bed is that the fluid phases are allowed to contact static surfaces as counter-current flow is induced by the rotating surfaces.

The essential idea is formation of thin layers of the heavy phase, driven by centrifugal effect, to increase heat and mass transfer rates. However, the computational work on a gas-liquid conical device of Makarytchev et al. (2004) suggests that mass transfer is dominated by gas contact with the spray droplets formed from the unstable liquid layer and at the rim of the rotating surface.

1.1 Principles and objectives

The differences between these various approaches can be understood only in terms of basic principles of counter-current contacting. These principles, which are present in the literature but are not all clearly prominent there, were developed precisely in MacInnes et al. (2012) for the case of the 'wide channel' model for rotating spiral flow and mass transfer. Here, it will be helpful to give a more simplified account of these principles in order to highlight the distinct advantages of the rotating spiral in relation to other approaches to centrifugal contacting.

First, decreasing the characteristic length, ℓ, for molecular diffusion in each phase increases the specific throughput, i.e. the throughput per device volume. Thus, for the same throughput and separation, small diffusion length reduces device size. Smaller geometric scale for the passages in a device along with increased body force (and hence velocity) can be used to reduce the diffusion length. The specific throughput achieved is roughly proportional to the inverse of the diffusion time scale, $\tau = \ell^2/\mathrm{D}$ where D is the diffusion coefficient. Thus, for example, if the characteristic size is reduced by a factor of 10 the device size is reduced by a factor of 100.

It is also important to control correctly the ratio of flow rates of the phases and the ratio of the phase element sizes, if efficient use of contacting volume is to be achieved. The optimum values of the relative element size and flow rate of the phases depend on the diffusion coefficients in the two phases and the equilibrium characteristics of the transferring solute in the two phases. A restriction on the relative flow rates of the phases is imposed by the equilibrium characteristics and the purification required. As an example, when transferring a solute from a gas stream into a liquid solvent stream in counter-current flow, the slope of the solute equilibrium curve sets a limit on the ratio of phase volume flow rates required to achieve a particular purification (e.g. Sherwood et al., 1975):

$$\frac{\mathrm{Q_V}}{\mathrm{Q_L}} < \frac{\mathrm{n_L}}{\mathrm{n_V}} \frac{1 - \mathrm{f'a_L}}{\mathrm{f'}(1 - \mathrm{a_V})} \qquad (1)$$

$\mathrm{f'}$ is the slope of the equilibrium curve of solute mole fraction in the processed stream (subscript V) as a function of mole fraction in the solvent stream (subscript L), Q is volume flow rate and n is mole density. The required purification is represented by $\mathrm{a_V}$, the ratio of solute mole fractions in the outlet and inlet of the processed stream, and $\mathrm{a_L}$ is the solute mole fraction in the solvent inlet stream (usually zero) relative to the inlet process stream mole

fraction. A flow rate ratio violating Eq. 1 cannot achieve the desired separation. On the other hand, an excessively small flow rate ratio is wasteful of solvent and there will be an optimum value of flow rate ratio. Each fluid contacting process (distillation, desorption, reactive separation etc.) will have a similar relation restricting the phase flow rate ratio in relation to purification and phase equilibrium. Thus, it is a basic principle of fluid phase contacting that the ratio of the phase flow rates is determined once the phase and solute system is fixed and the degree of separation is decided.

Finally, the optimum ratio of the phase diffusion lengths is dictated by the diffusion time scale in each phase ($\tau = \ell^2/\mathrm{D}$) and the velocity scale of each phase, $\mathrm{u} = \mathrm{Q}/\mathrm{A}$ (A is flow section area for the particular phase). The order of magnitude of the optimum relative size of the phase elements, $\ell_\mathrm{L}/\ell_\mathrm{V}$, is determined by requiring that the distance travelled in the diffusion time for each phase is the same (i.e. $\mathrm{u_V}\tau_\mathrm{V} = \mathrm{u_L}\tau_\mathrm{L}$) so neither phase restricts mass transfer more than the other. In order to arrive at a final relation, it is necessary to express A in terms of phase diffusion scale (ℓ) which requires knowledge of the particular geometry of space occupied by each phase and the state of flow in each phase. In the simplest case in which the phases flow in planar parallel layers (approximated by the rotating spiral flow considered here) ℓ corresponds to layer thickness, $\mathrm{A} \propto \ell$ and the following relation determines the order of magnitude of optimum relative size of the layers.

$$\frac{\ell_\mathrm{L}}{\ell_\mathrm{V}} = \frac{\mathrm{D_L}}{\mathrm{D_V}} \frac{\mathrm{Q_V}}{\mathrm{Q_L}} \tag{2}$$

Usual phase geometries for turbulent or intermittent flows are much more complex, involving droplets, bubbles, rivulets and films on complex solid surfaces, as well as viscous sub-layers. But, for each particular phase geometry one may encounter, it would be possible in principle to establish the relationship between phase section area and phase scales and thus arrive at a relation like Eq. 2 between relative element size and the flow rates and diffusion coefficients.

For the parallel-layer arrangement of the phases in laminar flow, Eq. 2 shows, as expected, that a relatively smaller element size will be required for the phase with the smaller diffusion coefficient. Also, the phase with the larger volume flow rate will require relatively smaller element size to decrease the diffusion time in that phase (as the element size is decreased the diffusion time decreases more rapidly than the velocity increases). Failure to satisfy Eq. 2 results in a longer distance travelled for the same mass transfer effect, and hence a larger apparatus to achieve the same purification. As mentioned, Eq. 2 can give only the order of magnitude of the optimum relative phase size. The precise optimum requires accounting for the detailed velocity and species mole fraction profiles in each phase layer, as is done with the wide-channel model in MacInnes et al. (2012).

Eqs. 1 and 2 highlight the fact that, to reach optimum fluid phase contacting, it is necessary to adjust independently the relative size of the phase elements and the relative phase flow rates. This is clear since equilibrium characteristics and diffusion characteristics are not in general (if ever) reliably correlated such that flow rates and element sizes satisfy Eqs. 1 and 2

simultaneously. Approaches which allow the phases to mix, including the rotating packed beds and probably also the spinning cones and discs, do not allow independent and detailed control over phase element size and flow rate ratio. The dynamics of the phase mixing that determines the phase geometries (e.g. bubble, drop or rivulet sizes) depend in a complex way on flow rates, passage geometry, driving forces and the density, viscosity, surface tension and contact angle properties of the phase system. Also, in the case of these rotating systems, centrifugal acceleration and section area vary radially such that even if optimum conditions could be achieved at one radial position they would not remain optimum throughout the contacting volume.

By contrast, the rotating spiral approach has the potential to allow full independent control of both the flow rates and the phase element sizes uniformly throughout the device. Furthermore, simple adjustment of rotation rate and pressure gradient allows optimum conditions to be achieved over a wide range of phase and solute systems in a single device. The phases do not mix and the contacting process remains largely independent of the interface properties (surface tension and contact angle on solid surfaces) of a particular phase system. While operation in the turbulent flow regime may in particular cases be advantageous, the laminar regime is considered here as it appears to have broader potential. These characteristics encouraged the development of a general-purpose experimental device allowing a broad program of testing and the resulting apparatus and initial hydrodynamic results are described here. With the results achieved, and further modelling of the phase interface shape, deviations between the wide-channel model and experiment are examined.

The two most important flow characteristics, according to both the wide-channel model and the discussion above in relation to Eqs. 1 and 2, are the relative thicknesses of the phase layers and the flow rate ratio of the phases. In the experiments with the new device, the flow rates are experimental inputs and the interface position is the remaining crucial variable to be measured. This is done photographically through a glass window covering the spiral channel using triggered strobe illumination and analysis of the recorded images. Results are obtained for gas-liquid flow over a range of phase flow rates and liquid viscosities. Comparison with the wide-channel model is made in each case to assess the model performance.

2 Apparatus

The design of the apparatus made extensive use of computations with the wide-channel model over broad ranges of liquid viscosity, phase density ratio and phase flow rate ratio. These computations guided the development and selection of components so the device could function as required over a long research life. Materials in contact with the fluids are either glass, PTFE, PEEK, 316L stainless steel, Viton (O-rings) and the carbon fibre-PTFE composite used for the rotating seals. The spiral element is modular so different designs can be used for different studies, e.g. smaller channel size might be used for effective liquid-liquid contacting, further inlets along the spiral would be needed for distillation or reactive

separations or interlaced and stacked channels might be used to demonstrate higher throughput.

Carbon fibre-PTFE lip seals (Ceetak Sealing Solutions) are used in pairs to form reliable connections between the shaft of the rotating unit and the stationary passages for each fluid stream. These individual connections allow independent control of each stream but introduce significant resistive torque and associated frictional heating. Computational analysis (2D and 3D using ANSYS Fluent) of the heat transfer based on estimates of the seal heat generation rate concluded that active cooling was required to maintain acceptable seal temperatures. On the basis of the computed results cooling water passages were incorporated into the shaft of the device to remove heat. Thus, a total of six seal pairs (two cooling water, two light phase and two heavy phase) are used in the device and the motor is sized to provide the necessary torque and power over the design operating range of about 500 to 5000 rpm (WEG 750 W three-phase induction motor and Invertek variable-frequency drive). The motor is oversized by about a factor of two for operation at the maximum seal pressure differential (4 bar) and highest rotation rate (4800 rpm). Practical production devices would operate at lower rotation rate with a stack of multiple channels supplied by common seal connections giving a far reduced power per unit flow rate. The process fluid itself may then be sufficient to cool the seals, thereby removing two seal pairs. Designs without any seals are also possible, thus leaving only the losses associated with the flow, shaft bearings, external aerodynamic resistance and those of the motor itself.

The apparatus is shown in Fig. 1 and comprises the drive motor, seal unit, spiral channel element (inset) and monitoring and imaging cameras with associated strobe light. Optical access to the spiral channel is through a bottom glass window used to cover and clamp the spiral element in place. The glass window also acts as a seal between adjacent revolutions of the spiral channel. This seal is not intended to be perfect but only to reduce the inter-channel leakage to total levels that are much lower than the liquid flow rate along the channel. (In practice tiny particles of seal debris block these seal paths after a period of operation following spiral element installation so leakage may be stopped altogether.)

Fig. 2 shows the flow network of the overall apparatus for both the contacting fluid pathways and the cooling water, for air-water contacting. Air is supplied from a compressor through a pressure regulator (REG 1); mains water is fed through a variable area flow metre and needle valve. The air leaving the spiral is passes through a filter to catch any liquid overflow before passing out to atmosphere through a further variable area flow metre and needle valve. The water exits the spiral to a 500 mL bottle in a ‘pressure pot’. Control of this downstream pressure determines the liquid pressure at the outer end of the spiral (see appendix) and hence, for gas-liquid contacting, the pressure throughout the spiral channel (the pressure gradient along the spiral when the light phase is a gas is generally negligible compared to the absolute pressure in the spiral). Once the spiral pressure is set in this way, phase flow rates are adjusted using the needle valves. Finally, the air supply pressure regulator must be adjusted so the pressure in the air flow at the outer end of the spiral matches that in the liquid outlet there, i.e. the air-water interface is positioned in the outlet reservoir as shown in the photograph on the right in Fig. 3.

The effect of liquid viscosity was tested using glycerol-water solutions or the ionic liquid [Emim][$EtSO_4$] in place of the mains water, giving a range of viscosity from about 0.6 to 60 cP. Nominal 60% and 88% (mass) glycerol in water solutions were used. The viscosity of each solution was measured directly to take into account effects of absorbed water or other impurities. Table 1 lists the densities and the measured viscosities (by gravity-feed capillary viscometry) at reference temperatures. Values at the spiral temperature were determined for water from available data and for the glycerol mixtures and the ionic liquid assuming the ratio of viscosities at the measured and spiral temperature were the same as for water. The viscous liquid flows were supplied using syringes and drives (Razel Scientific Instruments syringe pumps) feeding directly into the heavy phase inlet (B in Fig. 2).

Table 1. Viscosity and density of the experimental liquids.

	Water	60% glycerol	88% glycerol	[Emim][$EtSO_4$]
ρ (kg/m^3, 20 °C)	1000	1150	1230	1240
μ (cP, 30 °C)	0.805	6.53	73.8	59.3 (23 °C)

The air pressure adjustment required continuous visibility of the reservoir region and this was achieved using a monitoring camera (IDS UI-1220SE-M-GL with FUJINON HF25HA-1B/1.4 lens) triggered by a Hall-effect sensor. The camera was used in turn to trigger a strobe light (Omega HHT41, < 30 μs flash duration) with circuitry linking the Hall-effect chip, the trigger input to the camera and the strobe trigger output from the camera. A digital single lens reflex camera (Canon EOS 550D) fitted with a macro lens (Canon MP-E 65mm f/2.8 1-5X magnification) also made use of the triggered strobe light to record high resolution colour images of local sections of the channel for quantitative measurements of liquid layer thickness. Fig. 3 shows views of the inner and outer ends of the spiral during operation recorded with the imaging camera. The liquid layer can be seen clearly in each visible section of the spiral channel, beginning from the liquid inlet at the inner end of the spiral and ending at the reservoir at the outer end. The channel is 1.5 mm in height, 4 mm in depth (what is referred to as the 'width' direction) and is 0.91 m in length. The liquid layer shown is about 130 μm thick giving a ribbon of liquid 4 mm wide and almost 1 metre long. Menisci are produced where the air-liquid interface meets both the glass wall of the viewing window and the bottom wall of the channel. The bright band seen in the liquid layer is approximately the region of the meniscus at the glass surface.

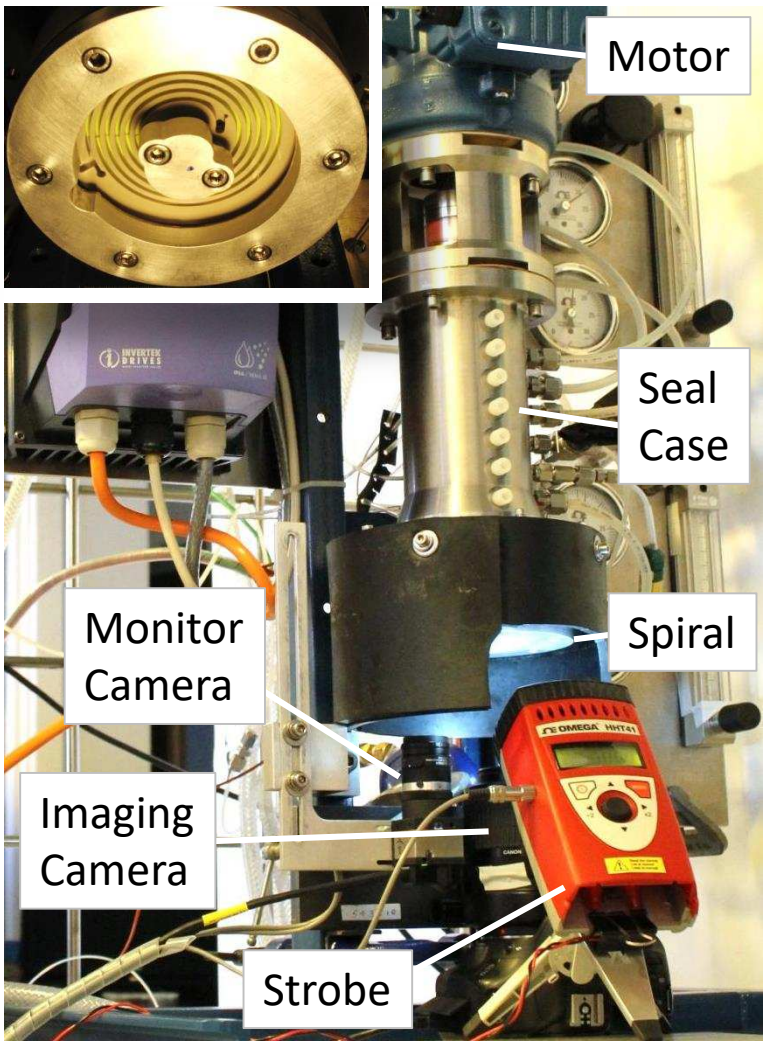

Figure 1. General apparatus showing the arrangement of the motor, seal unit, spiral channel (inset), cameras and strobe light. Flow connections can be seen along the right hand side of the seal case.

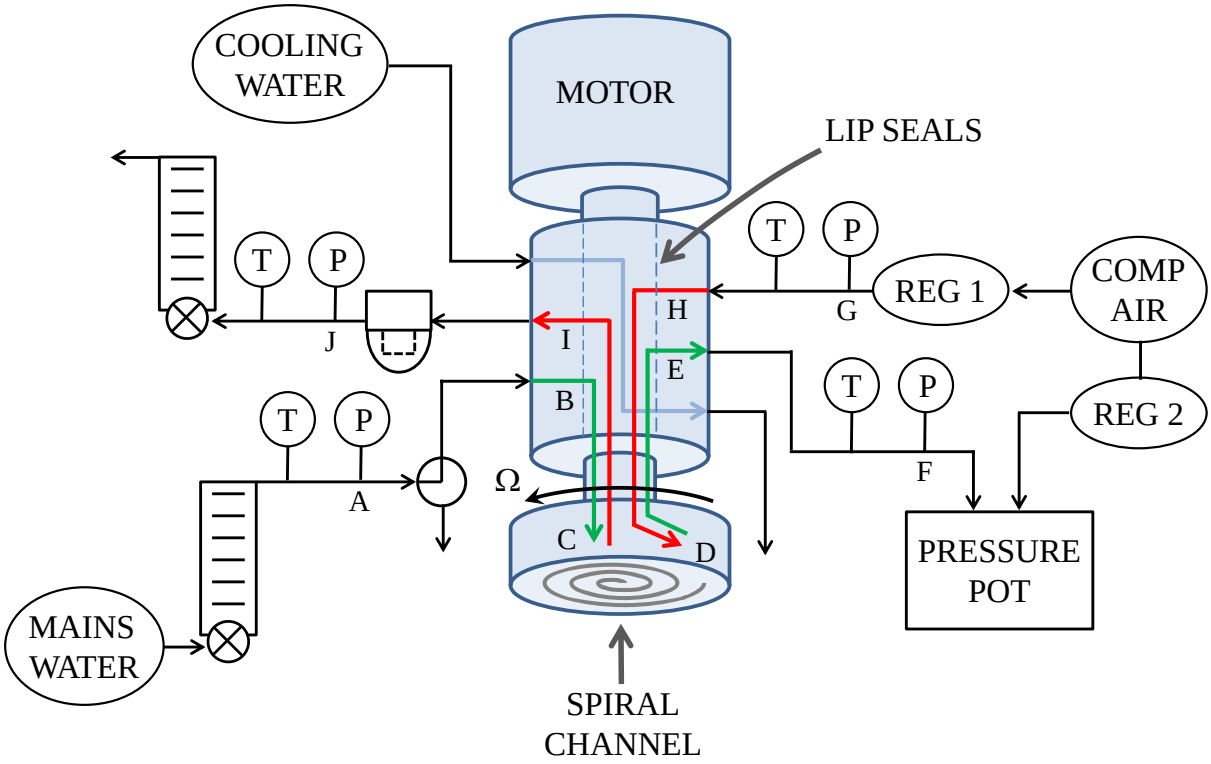

Figure 2. Schematic diagram of the flow network used for the air-water tests. Regulated compressed air flows from the outer end of the spiral (D) to the inner end (C) before returning to atmosphere via a needle valve and rotametre. Mains water (typically 43 psig) enters through a second rotametre to the inner end of the spiral, flows to the outer end (counter-currently to the air) and out to a collection vessel in a pressurised chamber (the 'Pressure Pot').

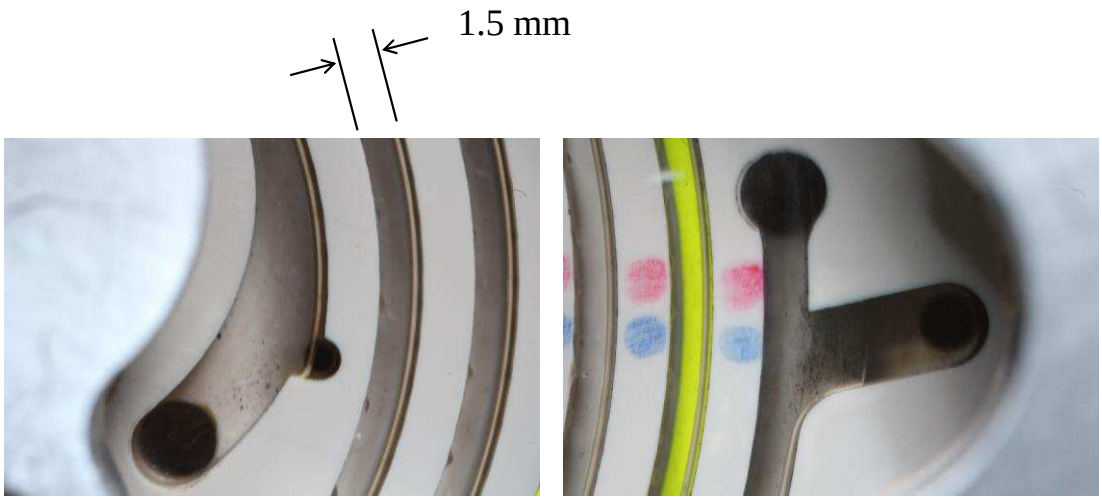

Figure 3. Photographs at the channel ends during operation with air and water at 2400 rpm (Q_V = 3.24 NL/min, Q_L = 8.93 mL/min, P_S = 2.1 bar absolute). The image on the left shows the inner end of the spiral, where the water enters and the air exits. On the right is the outer end of the spiral where air enters and water exits.

3 Wide-channel model

The analytical solution of Tilley et al. (1994) for developed two-layer flow between inclined parallel plates may be applied to flow in a rotating spiral by replacing gravitational acceleration with centrifugal acceleration. MacInnes et al. (2012) do this and extend the solution to include mass transfer of a dilute solute species. Provided the radius of curvature of the spiral channel is large compared to channel size, the spiral channel has a large aspect ratio (width to height) and centrifugal acceleration greatly exceeds gravity, this analytical theory is reliable for Newtonian and Fickian fluids. In practical designs, satisfying these conditions is expected to be possible and indeed may often be desirable. For the present experimental spiral the aspect ratio is relatively small (2.7) so channel end-wall effects are expected to produce significant from the model prediction in some cases.

The relevant aspects of the solution are the relations for the light-phase and heavy-phase flow rates (Q_V and Q_L, respectively) as functions of spiral pressure gradient, rotation rate, geometric parameters and the fluid properties:

$$Q_V = -\frac{h^3 w}{12\mu_V}\frac{dp}{dx}\left\{\frac{(1-\xi)^2\left[3(1-\gamma)\mu_r\xi^2 + (1-\rho_r\gamma)(1-\xi)(1-\xi+4\mu_r\xi)\right]}{1-(1-\mu_r)\xi}\right\} \tag{3}$$

$$Q_L = -\frac{h^3 w}{12\mu_V}\frac{dp}{dx}\left\{\frac{\mu_r\xi^2\left[3(1-\rho_r\gamma)(1-\xi)^2 + (1-\gamma)\xi(4(1-\xi)+\mu_r\xi)\right]}{1-(1-\mu_r)\xi}\right\} \tag{4}$$

$$\gamma = \frac{\rho_L R_O \Omega^2 \sin\alpha}{dp/dx} \tag{5}$$

Here h is channel height, w is channel width, R_O is radial position to the outer wall of the channel, α is the local spiral angle, $\rho_r = \rho_V/\rho_L$ and $\mu_r = \mu_V/\mu_L$, where ρ_L and μ_L are density and viscosity of the heavy phase, ρ_V and μ_V are light-phase density and viscosity. For given phase flow rates, rotation rate (Ω), channel height, spiral geometry and phase properties, Eqs. 3-5 can be solved to determine the spiral pressure gradient (dp/dx), the thickness of the heavy-phase layer relative to channel height (ξ) and the ratio of forces (γ). In the experiment, measurement of phase flow rates thus allows prediction of the heavy phase layer thickness and this can be compared with the measured layer thickness.

The phase densities and viscosities are determined using standard relations or data for these as functions of temperature and pressure. The temperature and pressure in the spiral are estimated as described in the appendix based on recording the transient of temperature at the exterior glass surface immediately following operation and using the liquid outlet passage as a manometer, respectively.

The path of the spiral is chosen such that $R_O \sin\alpha$ is constant along the channel, so the ratio of the forces driving the flow (γ), and hence contacting conditions, remain constant. The spiral path is most conveniently described in terms of polar coordinates for which the radial position (R_O), azimuthal angle (θ), and spiral angle (α) are related by the differential equation $dR_O/d\theta = R_O \tan\alpha$. In the experimental geometry α is sufficiently small (< 2° in the experimental spiral) for $\tan\alpha$ to be

replaced by $\sin\alpha$ on the right hand side. For constant $R_O \sin\alpha$ and noting that in one full spiral revolution, R_O must increase by $h+t$, where t is the wall thickness between adjacent revolutions of the channel. The equation for the channel path is that of an Archimedean spiral:

$$R_O(\theta) = R_O(0) + \frac{(h+t)}{2\pi}\theta \tag{6}$$

In the case of the present experimental channel, h = 1.5 mm, t = 2 mm, $R_O(0)$ = 16.5 mm, $R_O \sin\alpha$ = 5.57×10^{-4} m and the spiral extends to $\theta = 11\pi$ (5.5 revolutions), giving a maximum outer-wall radial position of $R_O(11\pi)$ = 36 mm.

In practice, the spiral is not perfectly centred on the rotation axis. The offset of the experimental spiral was determined by photographing it from below to establish the spiral centre (by comparison with the spiral design equation) and, without moving the camera, photographing a distinct mark on the spiral when rotating and using a long exposure, producing a circle in the image to establish the rotation centre. The spiral centre was determined to be offset 305 µm in the direction θ = 174°. This offset gives negligible correction to $R_O \sin\alpha$ at θ = 0, the position where the layer measurements were recorded, and the nominal value listed above was used in the wide-channel model predictions.

4 Interface model

In the experiment, and typically for rotating spiral contacting, the spiral angle is small and consequently the component of centrifugal force driving the flow along the channel is much smaller than the lateral component which determines hydrostatic pressure variation over the channel section and influences the interface shape. Since the viscous forces must balance the small component of centrifugal force along the channel, it follows that the interface shape is effectively independent of viscous stresses and thus is determined solely by the contact angles at the channel walls, the interfacial surface tension and the hydrostatic pressure variation in the fluid on either side. So the shape of the interface is not influenced by the phase flow rates or by changes in the heavy-phase layer thickness caused by changes in the flow rates. Further, the curvature of the interface in the transverse direction is far greater than that along the channel, which can therefore be neglected. Determining the shape of the phase interface thus reduces to solution of the Young-Laplace equation for interface pressure difference in terms of interfacial surface tension, σ, and radius of curvature, r, in the two-dimensional section of the channel:

$$P_V - P_L = \frac{\sigma}{r} \tag{7}$$

In terms of the coordinate system of Fig. 4, the pressure difference between the heavy-phase and the light-phase side of the layer ($P_V - P_L$) is given by

$$P_V - P_L = \Delta P_o + (\rho_L - \rho_V)\left[R_O\Omega^2 y - \mathbf{g}\cdot\mathbf{k}\, z\right] \tag{8}$$

The radial distance from the rotation axis to a given position on the interface has been taken as constant and equal to the radial distance to the outer wall of the channel, R_O. The excluded terms associated with this approximation have a negligible effect on the results since $R_O >> h$.

The radius of curvature in the Young-Laplace equation can be expressed in terms of arc length, ℓ, along the interface to give parametric equations for the coordinates of the interface surface. Normalising using channel height, h, Eq. 7 with Eq. 8 used to replace $P_V - P_L$ becomes (e.g. Salas and Hille, 1974):

$$\frac{d^2 y^*}{d\ell^{*2}} = \left\{ \Delta P_o^* + \left(\frac{h}{\delta_C} \right)^2 \left[y^* - \lambda z^* \right] \right\} \frac{dz^*}{d\ell^*} \tag{9}$$

$$\frac{dz^*}{d\ell^*} = \left[1 - \left(\frac{dy^*}{d\ell^*} \right)^2 \right]^{1/2} \tag{10}$$

The starred variables indicate normalised values with, for example, $y^* = y/h$, and the normalised pressure difference across the interface at $z = y = 0$ given by $\Delta P_o^* = h\Delta P_o / \sigma$. This non-dimensional representation shows that the shape of the interface depends on two parameters: the characteristic capillary height, δ_C, (Hunter, 2001) relative to channel height and the ratio of gravity and centrifugal acceleration, λ:

$$\frac{\delta_C}{h} \quad \text{where} \quad \delta_C = \sqrt{\frac{\sigma}{(\rho_L - \rho_V) R_O \Omega^2}} \qquad \text{and} \qquad \lambda = \frac{\mathbf{g} \cdot \mathbf{k}}{R_O \Omega^2} \tag{11}$$

In addition there are three non-dimensional geometric parameters affecting interface shape: the contact angles at the end walls of the channel, θ_G at the glass surface and θ_P at the plastic surface, and the channel width to height ratio, w/h.

The interface profile is calculated by numerical integration of Eqns. 9 and 10 starting from the point of contact with each end of the channel, where the slopes of the interface are known from the imposed contact angles. The initial pressure difference (ΔP_o^*) at the ends of the interface (one at each end) are adjusted such that the local pressure difference and interface slope are continuous where the two integrations meet. Explicit integration using 500 equal steps, $\Delta\ell^*$, from each end of the interface is found to produce results accurate to 0.1% (determined by comparison with results for meniscus heights using yet finer integration step size).

Since the solution is independent of liquid layer thickness and phase flow rates, the interface shape given by the model depends only on rotation rate and channel radial position, for given phase densities, surface tension, contact angles and channel width. Fig. 5 shows computed profiles for the water-air system used in the main experiments and in the outer revolution of the experimental spiral; corresponding values of capillary height and force ratio are listed in Table 2. To give a sense of scale, the interfaces are plotted such that the minimum liquid layer thickness is 100 μm ($y = 0$ corresponds to the outer channel wall, $z = 0$ to the bottom plastic channel wall and $z = 4$ mm is the glass window

surface). At high rotation rate, the capillary height is small enough that the menisci do not extend fully across the channel width, leaving a central region that is simply inclined such that it is perpendicular to the direction of the combined (centrifugal and gravity) body force vector. This tilt is clear in the plot with expanded scale (inset in Fig. 5). On the other hand, at low rotation rate the interface is continuously curved over the entire channel width. The division between these two regimes will depend on phase and channel properties. For the water-air system and the present spiral geometry, the results in the figure suggest that above about 2400 rpm the liquid layer thickness is approximately uniform over most of the channel width, while at lower rotation rate the menisci introduce significant variation in thickness.

The above model for the interface profile provides the basis both for determining the minimum layer thickness from photographic images and for interpreting the layer thickness results in relation to the wide channel model. For these purposes, measurements of surface tension (pendant drop method) and contact angles on the various experimental channel surfaces were carried out and the results (to the nearest 5° for contact angles) are summarised in Table 3. In the case of contact angles, measurements were made after the surfaces were exposed to tap water for several days to approximate the condition reached for these surfaces within the experimental channel.

Table 2. Dynamic parameter values for the air-water interface profiles computed in Fig. 5.

Rotation rate, Ω (rpm)	600	960	1480	2400	3840
Capillary height, δ_C (mm)	0.74	0.45	0.30	0.18	0.12
Acceleration ratio, λ	0.074	0.029	0.012	0.005	0.002

Table 3. Measured surface tension and contact angle values for the experimental liquids.

	Water	60% glycerol	88% glycerol	[Emim][$EtSO_4$]
σ (N/m)	0.07	0.064	0.068	0.046
θ_G	45°	40°	45°	55°
θ_P	75°	70°	75°	60°

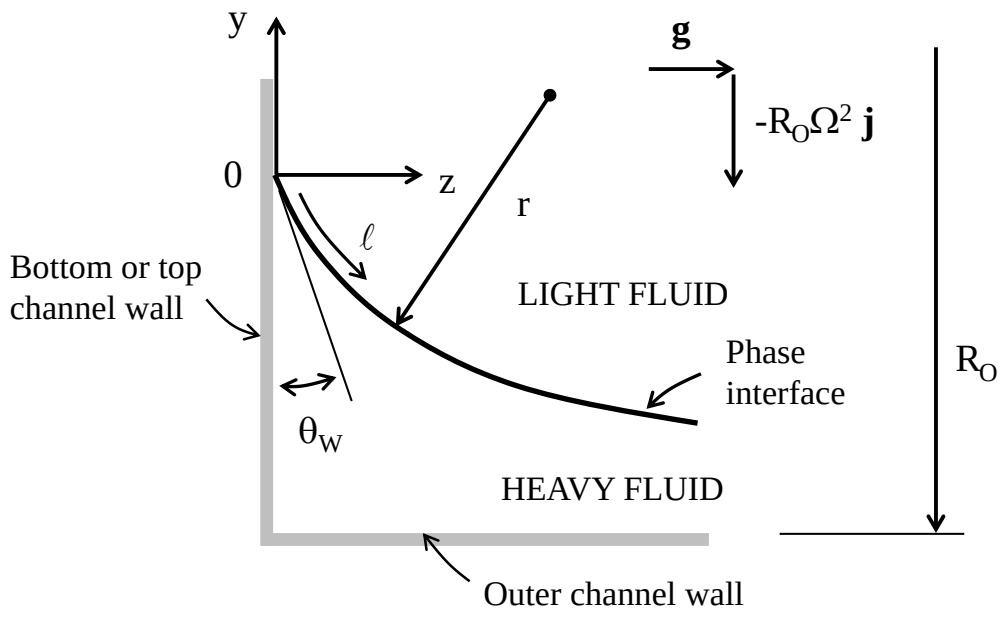

Figure 4. Geometry of the interface. R_O is the radial distance from the rotation axis to the outer channel wall. θ_W is the contact angle at the channel wall surface and represents either θ_G (at the glass wall surface) or θ_P (at the plastic wall surface, i.e. PEEK or yellow tape).

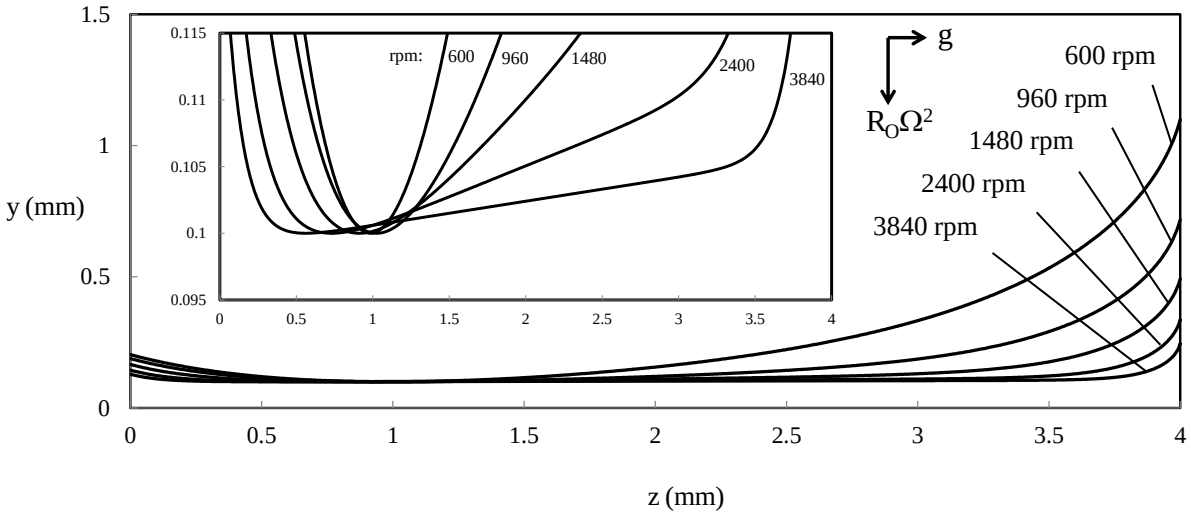

Figure 5. Computed interface profiles for air and water in the experimental channel at various values of rotation rate for conditions typical of the experiments. $z = 0$ corresponds to the plastic surface and $z = 4$ mm to the glass surface. The conditions are as follows: $\theta_G = 15°$, $\theta_P = 75°$; $\rho_L = 995$ kg/m^3, $\rho_V = 2.4$ kg/m^3 and $\sigma = 0.07$ N/m; $h = 1.5$ mm, $w = 4.0$ mm and $R_O = 34$ mm. The inset plot shows the same curves with an expanded y-coordinate scale.

5 Layer thickness measurement

The minimum liquid layer thickness and the meniscus height at the glass channel surface is determined using a combination of photography, image analysis and interface model calculations. Images are recorded with the imaging camera fixed to the support pedestal of the device and aligned such that the optical path to the outer channel wall is parallel to that wall. A Magnification of 1.25X was used with the maximum aperture setting of the lens (f16) to gain greatest depth of focus. This is important since features both at the near-end of the channel (rim edges and interface contact line on the glass) and within the channel (channel bottom and side reflected by the interface) need to be resolved. The use of the small aperture however resulted in considerable image noise for illumination with a single strobe pulse. Since the flow is steady in the rotating frame and the strobe flash is synchronised with the rotation, multiple flash exposures can be used to produce a single image. Typically, experimental images used 32 consecutive strobe flashes (rotations of the spiral). A study of numerous single-exposure images confirmed the flow to be steady and the flash to be well synchronised with rotation, with the typical standard deviation in the position of a given feature found to be around 4 μm. This deviation is the same as the pixel spacing in terms of recorded-image units. Thus, for example, the measurement uncertainty due to these factors is 4% for a 100 μm layer thickness.

Other errors arise from misalignment of the camera and image blurring during the strobe flash duration. Even at the longest duration indicated by the strobe manufacturer (30 μs), the transverse blurring due to rotation is 7 μm (at the highest rpm used in the tests). Concerning alignment of the optical path with the channel wall, the camera can be positioned to within about 100 μm and this would contribute an estimated error in the measured layer thickness of 2 μm. Thus, measured values of layer thickness presented here are expected to have an overall uncertainty of around 4 μm, rising to about 7 μm at the highest rotation rate used.

5.1 Image analysis

The above procedure leaves out an important aspect of correctly determining the minimum liquid layer thickness. Light reaching the camera from the interface near the minimum point is actually reflected light emitted by the channel walls. Since the liquid layer is thin compared to the channel width, the light from the walls arrives at the air-liquid interface with angles greater than the maximum refraction angle and the interface acts as a nearly perfect mirror. This causes a problem in practice: reflected light from the walls is of similar intensity and colour to that received directly from the walls and it is difficult to detect the interface outline. For this reason colour contrast between the side and bottom walls was introduced by covering the channel bottom with yellow fluorescent tape (Lynvale Adhesive Tapes). This measure does not improve detection of the interface outline, since direct light from the channel bottom is indistinguishable from light reflected from the channel bottom. However, what can be detected in the photographs is the point where the reflected yellow from the channel bottom changes to the brown colour reflected from the channel side (PEEK). The position in the image of this reflected corner can be measured and then the minimum liquid layer position (and hence its minimum thickness) can be determined using the shape calculated using the interface model.

Fig. 6a shows a typical photograph of the air and water layers, in which four distinct regions are seen. Two correspond to light from the channel bottom passing directly through a single phase within the channel, air on the left hand side and water on the right hand side. In between these is the image of the interface region, which divides into two sub-regions. To the left, light travels to the camera at an angle to the interface normal direction that is less than the maximum refraction angle. In this region

both refracted and reflected light contribute. On the right, the angle exceeds the maximum refraction angle and light passing to the camera is purely by reflection, giving an image of the channel side wall contacted by the liquid. One can see the striations resulting from cuts of increasing depth made by the milling tool to form the spiral channel.

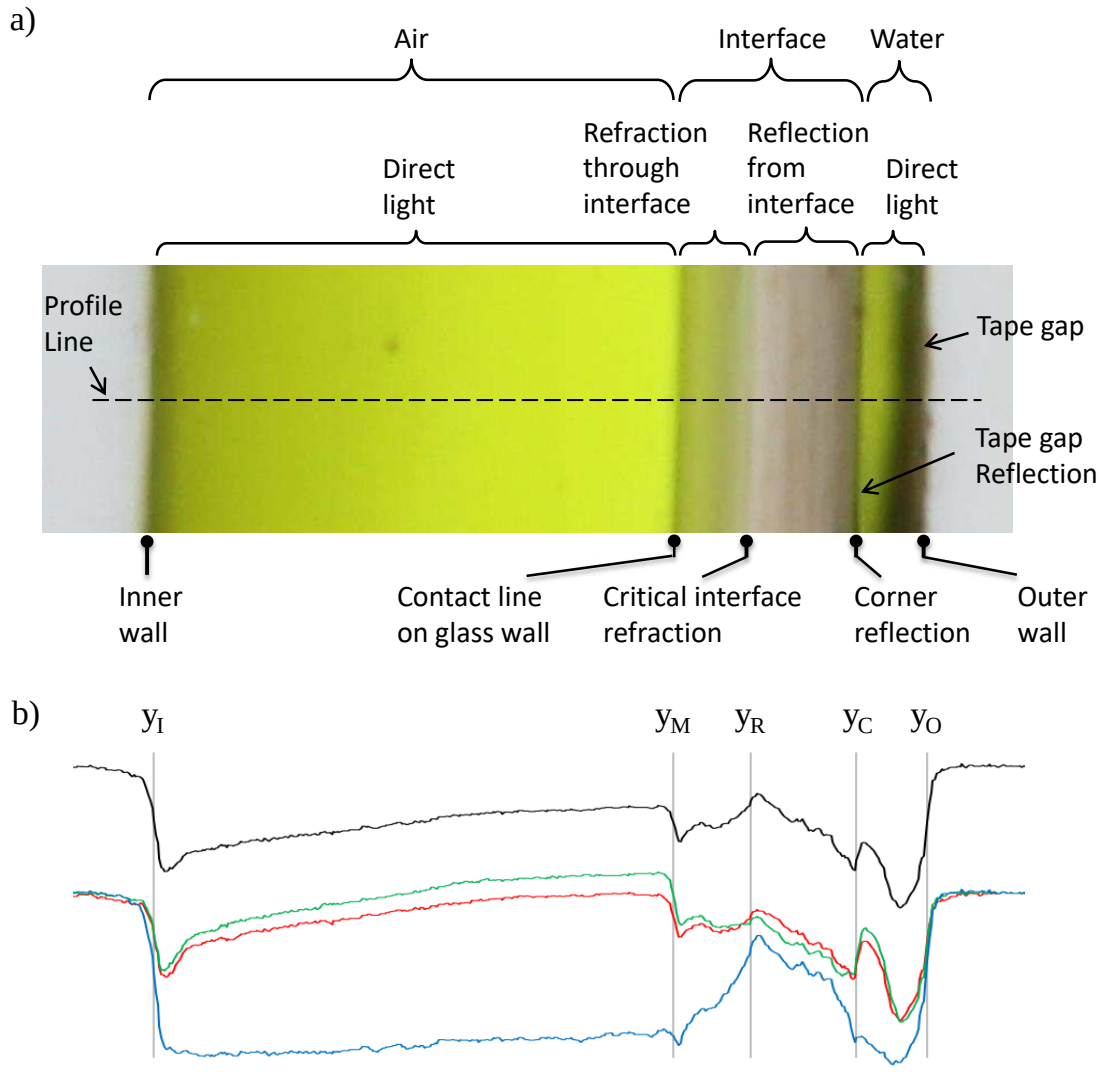

Figure 6. Detail of a typical photographic image of an air-water flow. Image with regions and key positions indicated (a) and RGB and monochrome intensity profiles along a the dashed line in the image (b). The positions of the inside wall, y_I, outside wall, y_O, glass contact line, y_M, critical refraction point, y_R, and corner reflection, y_C, are indicated on the intensity plot.

Fig. 6b shows light intensity profiles for the image taken along the dashed line in Fig. 6a. These are extracted from standard JPEG-format files produced directly by the camera software and comprise the three intensity arrays: red, green and blue. The key positions in the image were determined using the first spatial derivative of the 'monochrome' intensity (average of the three colour-channel intensities).

Each position is determined by location of the maximum absolute value of this derivative in the vicinity of a particular position. The inner and outer channel walls are characterised by a sharp decrease and increase, respectively, the glass contact line by a sharp drop in intensity and the corner reflection by a sharp rise to the strong yellow shade corresponding to direct and reflected light from the channel bottom. Identification of the point of critical refraction requires reference to the blue intensity which contributes weakly to yellow light. Thus, the critical refraction point is determined by the location where the blue light has recovered from a low intensity in the strongly yellow light of the refracting region to the higher relative intensity of the region that only reflects light from the PEEK side wall. It is debatable exactly where the critical refraction point lies, but the position of maximum derivative just to the left of the peak in monochrome intensity proved to be a robust and repeatable feature throughout the entire experimental range and was used in the analyses. It is interesting to note the decreasing level of blue light in the reflection region as the corner reflection point is approached. This can be explained by the increasing illumination of the PEEK channel side wall by yellow light emitted by the channel bottom.

5.2 Minimum layer thickness

The positions available from the photographic images do not include that of the minimum point in the interface profile, y_L, or the meniscus height ($h_M = y_M - y_L$). The minimum position can, however, be determined from the measured corner-reflection position, y_C, using the theoretical interface shape, assuming the interface model is a faithful account of the experimental interfaces. To test this, the profile used to determine y_L can also be used to predict the measured meniscus height and the position of the critical refraction point, y_R. The interface profile is calculated individually for each experimental point according to the particular conditions of radial position, rotation rate and fluid properties that apply. h_L is determined by varying its value with the model interface profile such that the calculated image position of the corner reflection matches that measured. Referring to the light-ray diagram and nomenclature in Fig. 7, position y_C is determined from the calculated interface shape by locating the interface position (z_C, y_C) where the calculated slope satisfies $(dy/dz)_C = \tan\theta_C$ and $\tan 2\theta_C = y_C / z_C$. Position y_R is determined by locating the interface position (z_R, y_R) where $(dy/dz)_R = \tan(\pi/2 - \theta_{max})$; θ_{max} is the maximum refraction angle for the interface. In the calculations of the air-water interface, the index of refraction of water is taken as 1.33, which represents a mid-wavelength of visible light in the experimental temperature range 30-40 °C, giving θ_{max} = 48.8° in that case. It is noted that the difference between the corner reflection position and that of the actual liquid layer minimum can be as much as 30% or more and as little as a few percent depending on interface shape and liquid layer thickness.

Fig. 8 shows predicted and measured meniscus and critical refraction positions relative to the minimum interface position plotted as functions of the capillary height. All data for the experiments with air and water are plotted and thus a wide range of liquid layer thickness, radial position and phase flow rates is represented. The curves in the plot show these relative positions as determined by the interface model. While the measured values show considerable scatter, the interface model clearly gives an excellent prediction of the critical refraction position. In the case of meniscus height, use of the measured contact angle on the glass surface gave meniscus heights very close to the refraction

heights, since the measured angle ($\theta_G = 45°$) is only slightly larger than the interface angle of 41.2° corresponding to critical refraction. With negligible effect on the predicted refraction position, a smaller glass contact angle ($\theta_G = 25°$ used for the curve shown in the plot) brings the model prediction for meniscus height closer to the measured values. Regardless of glass contact angle, the measured meniscus heights increase with capillary height less rapidly than in the model. These discrepancies are perhaps not surprising since the meniscus height may depend sensitively on further processes not included in the model such as evaporation or heat transfer which, however slight, may strongly affect the thinning layer of liquid as the contact line is approached. This could impose an effectively reduced near-wall interface angle with the reduction depending on capillary height and flow rates. Fortunately, the agreement for critical refraction position is clear and this gives strong support for the accuracy of the predicted profile shape in the central part of the interface and, hence, of the determination of minimum layer height (h_L) from measured corner reflection position (y_C). The close correspondence between the capillary height parameter (Eq. 11) and the measured meniscus height is clear from the plot, with meniscus height found to be about 15% greater than the capillary height.

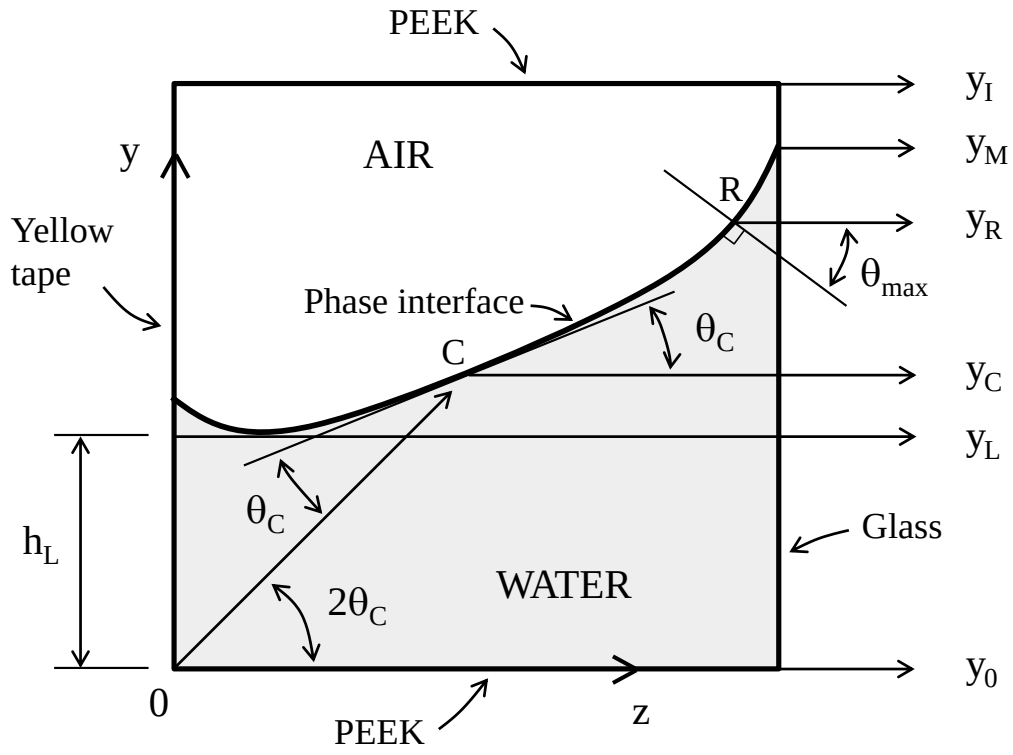

Figure 7. Light paths to the camera associated with identifiable positions in the photographs (diagram not to scale of the experimental channel).

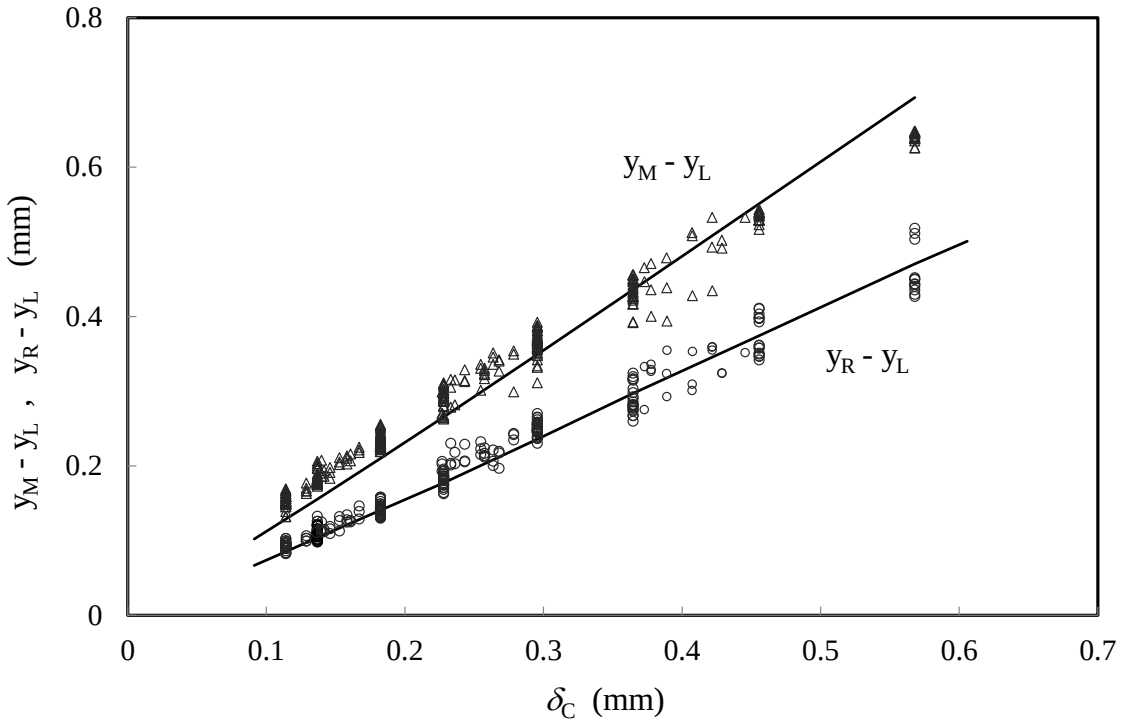

Figure 8. Comparison between measured and calculated interface height parameters as functions of the capillary height. Symbols are measurement (triangles, meniscus height; circles, critical refraction height) and the solid curves are calculation using contact angles $\theta_P = 75^\circ$ and $\theta_G = 25^\circ$. The measurements are for air-water flow and include all data over the entire range of flow, radial position and rotation rate.

6 Air-water results

Applying these measurement techniques to air-water contacting in the apparatus, the effect on liquid layer thickness of rotation rate and phase flow rates can now be determined. The strong effect of rotation rate on both layer thickness and meniscus height can be seen in the channel section images in Fig. 9. The flow rate of each phase remains constant, so the changes from image to image are due solely to rotation rate. As rotation rate increases, the centrifugal body force driving the liquid against friction ($\rho_L R_0 \Omega^2 \sin\alpha$) and that restraining it against surface forces ($\rho_L R_0 \Omega^2 \cos\alpha$) also increase. So in the figure liquid layer thickness decreases with rotation rate since the increasing driving force per unit volume can balance an increasing wall shear stress as the same flow rate passes through a smaller section area. The meniscus height also decreases due to the increasing lateral centrifugal body force. Debris from seal wear can be seen especially at the outer wall where it has settled due to its high density relative to the fluid phases. The presence of the seal debris had no effect on controlling the layers and flow, although the spiral element was periodically disassembled and cleaned to give clear images for the quantitative image analysis.

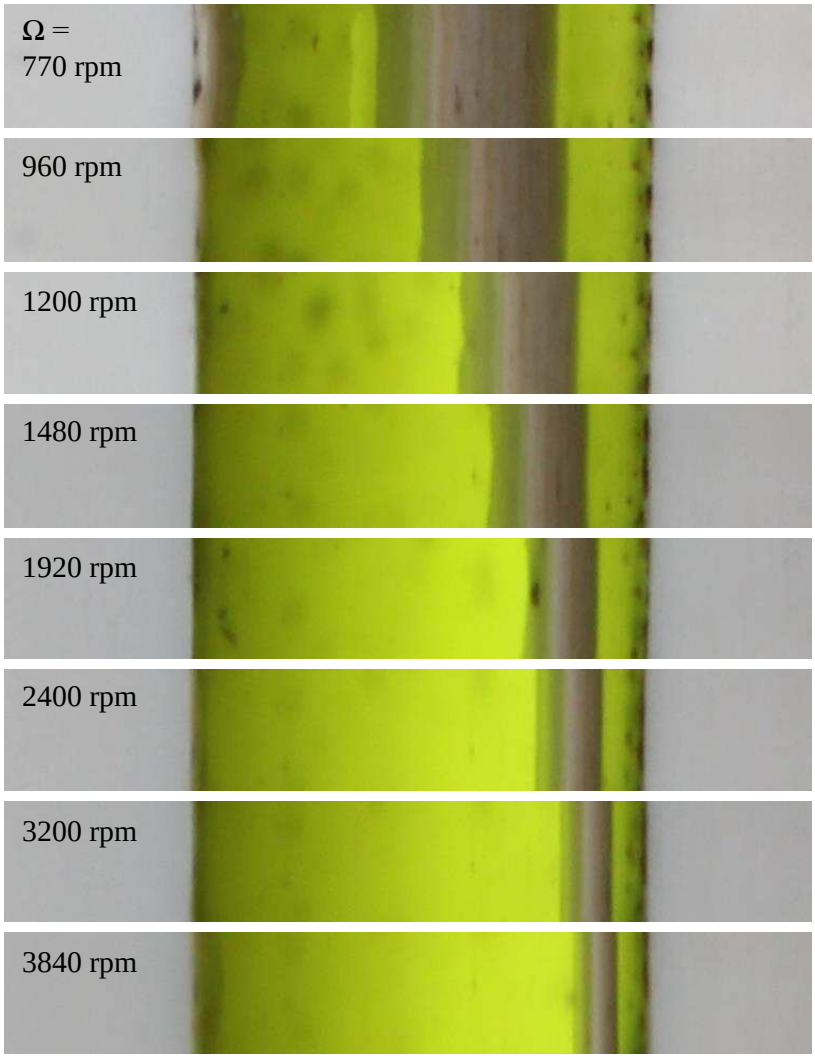

Figure 9. Liquid layer thickness and meniscus size variation with rotation rate for the air-water system. Images are taken near the outer end of the channel at R_0 = 34 mm and the phase flow rates are fixed at Q_V = 1.71 NL/min and Q_L = 9.60 mL/min.

6.1 Effect of phase flow rates

Fig. 10 shows minimum liquid layer thickness over a range of air flow rate at four different rotation rates at fixed liquid flow rate (Q_L = 9.60 mL/min). The symbols represent the measured values and the solid lines are the prediction of the wide channel model. The model captures the measured layer thickness well at high rotation rates but less well as rotation rate decreases. Agreement is perhaps also slightly less good at lower gas flow rates. It is clear though, either experimentally or according to the model, that the gas flow has a relatively minor effect on liquid layer thickness. For gas-liquid contacting, the liquid flow is driven primarily by the centrifugal body force against the resistance of wall shear stress, with pressure gradient and gas shear stress at the interface generally playing minor role. The order of magnitude of the interface shear stress relative to the wall shear stress is readily estimated for these laminar flows:

$$O\left(\frac{\mu_V}{\mu_L}\frac{Q_V}{Q_L}\frac{h_L^2}{(h-h_L)^2}\right) \tag{12}$$

For the conditions of the figure, the viscosity ratio is about 10^{-2}, the ratio of flow rates varies from zero up to about 400 and the ratio of phase layer thicknesses ranges from 0.07 at high rotation to 0.2 at the lowest. At high rotation rate, these give an overall magnitude for the interface shear stress that is less than 2% of the wall shear stress contribution, even at the highest gas flow rate. Hence, the negligible effect of gas flow rate on the liquid layer seen in the results at high rotation rate. At low rotation rate, the liquid layer thickens, wall shear stress is decreased and interface shear stress is increased so the gas flow has a significant effect. Even at one half the maximum gas flow rate, the magnitude of the interface shear stress rises to 16% of the wall stress at the lowest rotation rate according to Eq. 12.

It can also be noted in the figure that the data extend to a maximum value of Q_V that decreases as rotation rate is decreased. Beyond this maximum value, the liquid layer thickens to an extent that liquid flows with the gas out through the gas outlet passage. So for example, it is not possible with the current spiral element design to operate at 960 rpm with the water-air system above a gas flow rate of about 3 NL/min at 9.6 mL/min liquid flow rate. Generally for the experimental spiral element, this overspill occurs for liquid layer thickness exceeding about 200 µm. It is expected that this limitation can be removed with suitable modification of the liquid inlet design. The current design was made with the knowledge that for gas-liquid contacting, the liquid layer thickness producing optimum mass transfer is typically well below 10% of channel height (MacInnes et al., 2012), i.e. for layer thickness less than about 150 µm for this experimental channel.

Measured meniscus height in the case of both Q_L = 9.60 mL/min and a lower liquid flow rate (3.49 mL/min) is shown in Fig. 11 along with the prediction of the interface model. The agreement is good and, as expected, the phase flow rates have no effect on meniscus height.

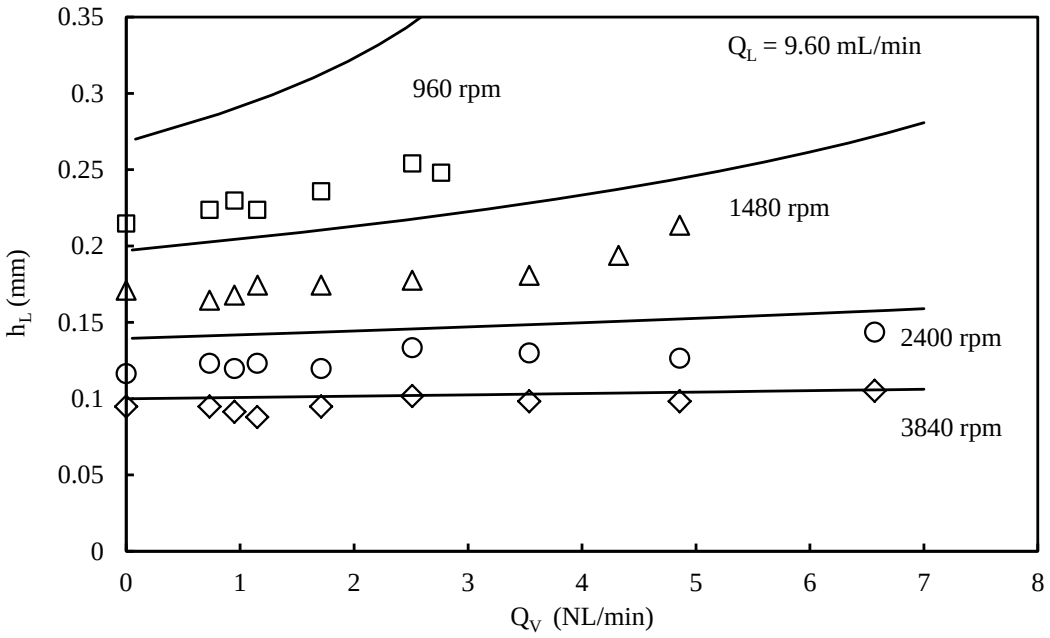

Figure 10. Measured (symbols) and predicted (curves) minimum liquid layer thickness over a range of air flow rate and rotation rate at fixed water flow rate (9.60 mL/min) and at 2.1 bar spiral pressure.

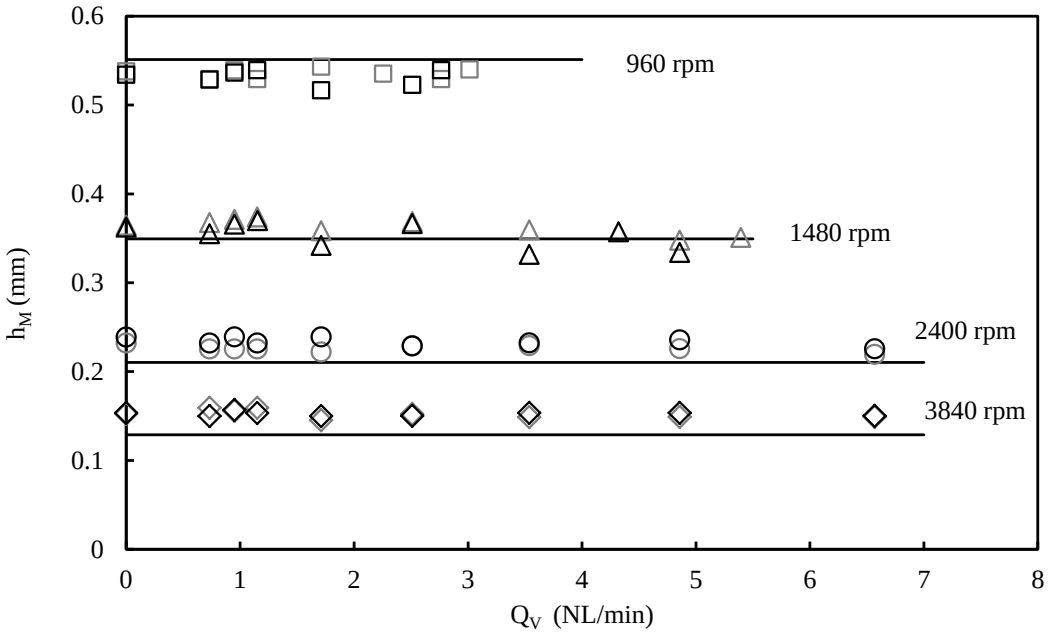

Figure 11. Measured (symbols) and predicted (curves) meniscus height at the glass channel wall. Black symbols are Q_L = 9.60 mL/min and the grey symbols are Q_L = 3.49 mL/min.

The tendency for a reduced liquid layer thickness in the experiment relative to the wide channel model can be explained in terms of the finite width of the experimental channel. Where the gas and liquid layers meet the end walls, two effects occur that cause deviation from the wide channel model. First, fluid motion is retarded relative to the free layer and, second, the liquid layer thickness is increased by formation of a meniscus (wetting conditions applying here). As mentioned, the calculated interface profiles for the experimental channel shape (Fig. 5) suggest that for rotation rate below about 2400 rpm the meniscus size is large enough to produce significant deviation from the uniform liquid layer thickness assumed in the model. While the change to the flow section of the gas phase is minor, the liquid section can be considerably altered by the end effects with thickened end regions and thinned central layer. Liquid then flows preferentially in the meniscus regions where the section area is large and the characteristic velocity is higher because of greater characteristic distance from the solid walls.

Thus, it appears that the wide channel model gives an accurate prediction of liquid layer thickness when meniscus height is small in relation to layer thickness. This will be the case either for large liquid layer thickness (high liquid flow rate, high gas flow rate) or for small meniscus height (high rotation rate, low surface tension, contact angles approaching $\pi/2$). The results for Q_V and rotation rate variation in Fig. 10 support this assessment since closest agreement is indeed found for large rotation rate (small meniscus height) and large liquid and gas flow rates (thicker liquid layer).

Further support for this idea is found when Q_L is reduced towards zero flow rate. Fig. 12 shows the result of variation over a wide range of liquid flow rate at an intermediate, fixed value of gas flow rate and for three different rotation rates. For large liquid flow rates the pattern of agreement between model and experiment is as before with rotation rates of 2400 rpm and larger providing sufficient suppression of meniscus height in relation to liquid layer thickness for the layer to approximate the uniform thickness assumed in the model. But at decreased low liquid flow rate the layer thickness is significantly reduced while the meniscus height remains unchanged at a given flow rate. Thus, below a liquid flow rate of about 2 mL/min, the experimental layer thickness becomes increasingly reduced comparted to that predicted by the model, even at high rotation rate.

The agreement should be improved by reducing the surface tension of the interface which decreases meniscus height (Eq. 11). This was confirmed by repeating the experiment with surfactant added to the water (0.5 g/L Fairy Liquid). The surface tension and contact angles were measured for this solution (σ = 0.024 N/m, θ_G = 5° and θ_P = 20°), conditions for which the interface model predicts a meniscus height reduction of about 25% for this solution relative to water. Because the contact angles for the surfactant solution are much smaller than for water, the effective meniscus height reduction for the surfactant solution is probably closer to the 42% due to surface tension alone (Eq. 11). The result for the experiment at 1480 rpm is shown with grey triangles in Fig. 12. The surfactant solution brings the experiment closer to the model as expected.

Fig. 12 shows that liquid layer thickness below 20 µm has been achieved according to the measurements. That such small thickness can be controlled over a channel width 200 times that thickness and a length 45,000 times that thickness comes as a surprise. It was thought that routine fabrication tolerances (of say 50 µm) would not allow layer thicknesses less than around 100 µm to be achieved. This is significant since, for this 1.5 mm experimental channel, calculations using the wide channel model suggest optimum gas-liquid contacting conditions are achieved for liquid layer thickness in the range 12 µm to 90 µm depending on the transferring solute properties, with even thinner layers optimum for viscous (low diffusion coefficient) liquids.

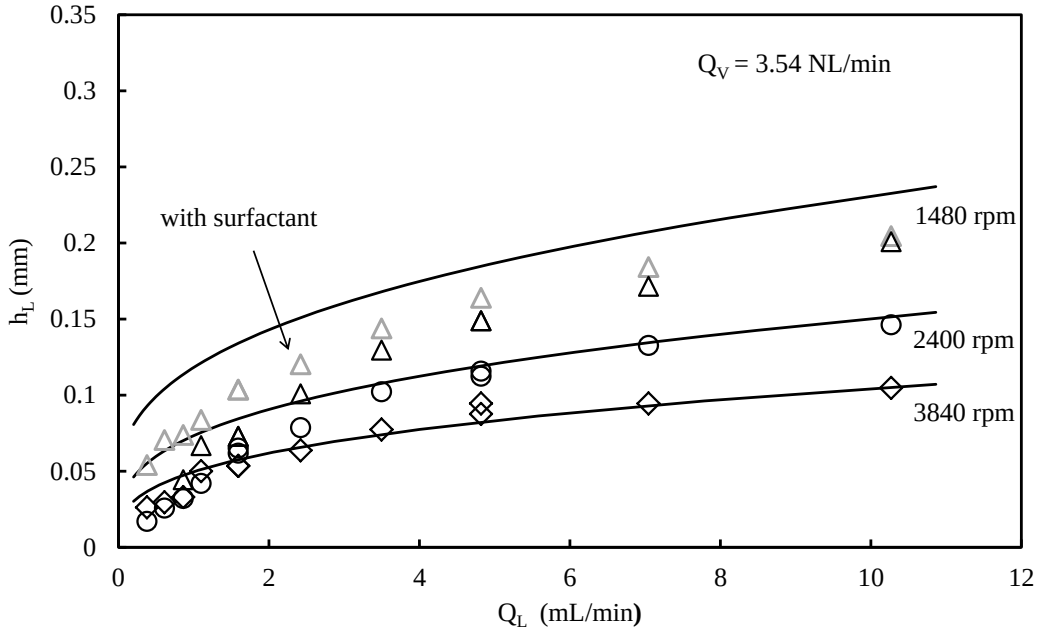

Figure 12. Measured (symbols) and predicted (curves) minimum liquid layer thickness over a range of water flow rate and rotation rate at fixed air flow rate (3.54 NL/min) and at 2.1 bar spiral pressure. (Grey triangles show the effect of surfactant at 1480 rpm.)

7 Viscous liquids

A generally-useful contacting device needs to handle the full spectrum of fluid phase properties. For gas-liquid contacting the most important property to consider is liquid viscosity. This viscosity can vary by orders of magnitude depending on the liquid and the temperature. To test the effect of liquid viscosity, glycerol-water mixtures and the ionic liquid [Emim][$EtSO_4$] were used in place of water to give a range of viscosity up to just over 70 times that of water (Table 1). Air flow rate, rotation rate and spiral pressure were held constant at 1.15 NL/min, 3200 rpm and 2.1 bar, respectively. Since, at fixed centrifugal driving force, the liquid flow rate must be decreased with increasing viscosity to maintain reasonable (ultimately optimum) liquid layer thickness, a syringe pump was used to drive these viscous liquids at the lower flow rates. The pump used had a range of linear velocity from 0 to 4 mm/min and this was used with 0.25, 1, 3, 5, 10 and 20 mL (luer-lock) syringes to span the required range of flow rates.

Fig. 13 gives measured minimum liquid layer thickness versus liquid flow rate for the various liquids. A logarithmic flow rate axis is used to allow the required three orders of magnitude spanned by the data to be shown on a single plot. The model (solid curves) captures the effect of viscosity well and, as before, over-predicts the layer thickness as the liquid layer becomes thin. It can be noted that the contact angles and surface tension values of the glycerol-water mixtures do not differ significantly from those of water (Table 3), so meniscus heights are approximately the same for these liquids. The ionic liquid has a somewhat lower

surface tension value (though similar contact angles) corresponding to just a 20% reduction in meniscus height relative to the other liquids. For each liquid the experiment begins to depart from the model prediction beginning at about h_L = 60 µm and as liquid layer thickness is reduced below this level the measured thickness falls progressively further below the predicted thickness in a similar manner for all of these liquids. Indeed, the data should collapse approximately when layer thickness is plotted versus $Q_L \mu_L$. That is, flow rate needs to decrease in inverse proportion to viscosity for a given layer thickness to be maintained. The inset in Fig. 13 shows the data collapse when this scaling is used. The model predicts the collapse to be only approximate as indicated by the two somewhat differing solid curves in the inset which represent the extremes of water and 88% glycerol-water in the normalised flow rate coordinate (upper curve is water; lower curve is the glycerol mixture). This is an expected consequence of the increased interface shear stress due to the high velocity of the water relative to that of the glycerol mixture for the same layer thickness and is broadly reflected in the data. It can be noted that the results for the concentrated glycerol mixture show considerable scatter, with several points falling above the model prediction. This is believed to be the effect of slight evaporation of water within the mixture resulting in considerable increase in viscosity for this case. The non-volatile ionic liquid and the lower concentration glycerol solution show no such tendency.

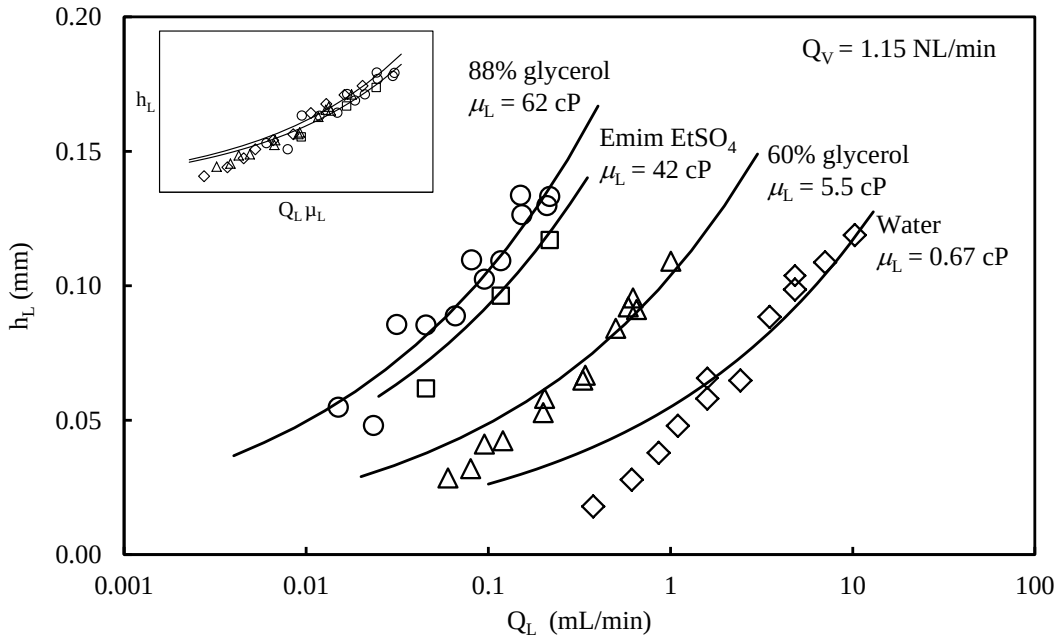

Figure 13. Measured and predicted liquid layer thickness for several liquids of differing viscosity at 3200 rpm as liquid flow rate is varied. Air flow rate, rotation rate and spiral pressure (2.1 bar) remain constant.

9 Discussion

The work presented demonstrates the effectiveness of the rotating spiral to control fluid phase contacting over a broad range of conditions. By changing the rotation rate and the flow rates,

the interface position in the channel and hence the relative thickness of the phase layers can be changed, as required to achieve optimum mass transfer. While no mass transfer measurements are reported here, this work on hydrodynamic aspects of the contacting flows lays the necessary experimental foundation for such studies. Mass transfer data over a wide range of phase and solute systems for dilute solute concentrations is obviously possible with the device since, with dilute concentration, the solute does not alter the physical properties (viscosity and density) that determine the flow. Furthermore, it is likely that the results presented can usefully inform application of the rotating spiral to more complex processes such as distillation, biphasic reaction with separation or cases where property non-uniformity accompanies variations in species concentration and temperature.

The wide-channel model (MacInnes et al., 2012) has predicted all of the experimental trends well, with the differences attributable to limitations due to the assumption of infinite width in the model. This assumption can be relaxed in the model to allow an account that resolves the shape of the interface (as calculated here) and the effect of the end walls in finite-width channels. This fuller model has been presented in a conference paper (Ortiz-Osorio et al., 2009) where calculations for the specific experimental conditions of MacInnes et al. (2010) were made. This model significantly increases the amount of work required to make progress towards a general understanding of rotating spiral performance, since numerical solution is required. Consequently, subsequent modelling work has focused on the wide-channel analytical model that forms the basis for the work reported here. The fuller model can be a powerful tool to understand quantitatively the deviations from infinite width flow behaviour in actual finite-width rotating spiral channels, including the well-known Coriolis secondary flows (Mori and Nakayama, 1968; Miyazaki, 1971; Draad and Nieuwstadt, 1998; Ishigaki, 1999; Lee and Baek, 2002).

The question of stability of the layers in rotating spiral flow is raised in MacInnes et al. (2012) since this limits the flow rate that can be obtained in a given channel and phase and solute system. In that work, critical values of Reynolds, Froude and Weber numbers were suggested to allow rough estimation of the achievable flow rates. Conservative values were suggested to avoid over-inflating the prospects of the technology. So it is worth noting that the range over which stable layer flow has been observed for the data reported here considerably exceeds the limiting criterion previously suggested. The highest gas flow rates represented in the data correspond to a Reynolds number of 1960 which is far greater than the conservative critical value of 500 suggested in our previous work, giving four times the flow rate. Also, Froude numbers as high as 0.8 are represented which is greater than the conservative critical value of 0.5 suggested previously.

Even so, it needs to be recognised that flow rates through the experimental channel are small. The liquid flow rate has been increased stably up to around 20 mL/min and the gas flow rate to around 10 NL/min, beyond which spatially-periodic interface waves occur and eventually control of the phase layers is lost. Focusing on the upper limit of gas flow rate, this device can therefore process up to about 15 kg/day of gas. By stacking multiple channels identical to the experimental channel, all fed by the same (but enlarged) set of passages, a throughput of about 1 tonne/day of gas in a unit measuring around 40 cm high and 15 cm diameter

appears to be possible. Such processing flow rates are believed to be suited to many requirements in applications involving fine chemical production. Of course, analytical applications generally would be handled by just a single channel.

10 Conclusions

The paper describes a prototype device representing the first successful general-purpose fluid phase contacting device using a rotating spiral channel. Gas-liquid contacting is examined with layer thickness measured using a technique based on digital photography and image analysis using a model for interface shape. The method has successively resolved liquid layers down to sub 20 µm thickness.

Measurements are made over a wide range of flow rates, rotation rates and phase properties (density and viscosity) and the experimental trends are captured well by the existing 'wide-channel' model. The results are for gas-liquid contacting and, as was known from model calculations for such systems, the liquid layer thickness increases with increasing liquid flow rate, gas flow rate and liquid viscosity while increasing rotation rate decreases the liquid layer thickness. It can be concluded that the parameters under external control – rotation rate and pressure gradient – can be used to set relative phase layer thicknesses and flow rates for optimum mass transfer over a wide range of different phase and solute systems.

The wide-channel model under-predicts liquid layer thickness when the end-wall meniscus heights are large relative to layer thickness and for such conditions accurate prediction requires a model that includes interface shape and end-wall effects. Still, the wide-channel model remains a valuable tool for identifying and judging the relative effects of design parameters.

The work opens the way for application to mass transfer processes such as absorption, distillation and reactive separation in gas-liquid systems. In the first instance mass transfer studies with the prototype device need to be carried out. The model suggests similar application to liquid-liquid contacting is possible and this direction can also be explored with the device developed here.

Acknowledgements

The Libyan government provided support for M. K. S. Zambri during his Ph.D. studies that enabled this research work to be undertaken and completed.

References

Anderson, D. W. and E. F. Lau, 1955, Commercial Extraction of Unfiltered Fermentation Broths in the Podbielniak Contactor, Chemical Engineering Progress, 51 (11), 507-512.

Barson, N. and Beyer, G. H., 1953, Characteristics of a Podbielniak Centrifugal Extractor, Chemical Engineering Progress, 49 (5), 243-252.

Buhtz, E., 1927, Method of and Apparatus for Carrying Out Chemical Reactions or Physical Processes, U. S. Patent 1,629,200.

Bruin, S., 1969, Velocity Distributions in a Liquid Film Flowing over a Rotating Conical Surface, Chemical Engineering Science, 24, 1647-1654.

Burns, J. R., Ramshaw, C. and R. J. Jachuck, 2003, Measurement of Liquid Film Thickness and the Determination of Spin-up Radius on a Rotating Disc Using an Electrical Resistance Technique, Chemical Engineering Science, 58, 2245-2253.

Draad, A. A. and F. T. M. Nieuwstadt, 1998, The Earth's Rotation and Laminar Pipe Flow, Journal of Fluid Mechanics, 361, 297-308.

Huffman, J. R. & Urey, H. C., 1937, Separation of Oxygen Isotopes by a Fractionating Column, Industrial and Engineering Chemistry, 29 (5), 531-535.

Hunter, R. J., Foundations of Colloid Science, Second Edition, Oxford University Press, 2001.

Ishigaki, H., 1999, Laminar Convective Heat Transfer in Rotating Curved Pipes, JSME International Journal, Series B, 42 (3) 489-497.

Jacobsen, F. M. and G. H. Beyer, 1956, Operating Characteristics of a Centrifugal Extractor, A.I.Ch.E. Journal, 2 (3), 283-289.

Kaiser, H. R., 1955, Dephenolizing of Wastes and Other Liquors by Centrifugal Solvent Extraction, Sewage and Industrial Wastes, 27 (3), 311-320.

Lee, G. H. and J. H. Baek, 2002, A Numerical Study of the Similarity of Fully Developed Laminar Flows in Orthogonally Rotating Rectangular Ducts and Stationary Curved Rectangular Ducts of Arbitrary Aspect Ratio, Computational Mechanics, 29, 183-190.

Kuvshinov, D., M. R. Bown, J. M. MacInnes, R. W. K. Allen, R. Ge, L. Aldous, C. Hardacre, N. Doy, M. I. Newton and G. McHale, 2011, Thermal Conductivity Measurement of Liquids in a Microfluidic Device, Microfluidics and Nanofluidics, 10 (1), 123-132.

MacInnes, J. M., Ortiz-Osorio, J., Jordan, P. J., Priestman, G. H., & Allen, R. W. K., 2010, Experimental Demonstration of Rotating Spiral Microchannel Distillation, Chemical Engineering Journal, 159 (1-3), 159-169.

MacInnes, J. M., M. J. Pitt, G. H. Priestman and R. W. K. Allen, 2012, Analysis of two-phase contacting in a rotating spiral channel. Chemical Engineering Science, 69, 304-315.

MacInnes, J. M., Z. Chen and R. W. K. Allen, 2005, Investigation of Alternating-Flow Mixing in Microchannels, Chemical Engineering Science, 60, 3453-3467.

Makarytchev, S. V., T.A.G. Langrish and R. G. H. Prince, 1998, Structure and Regimes of Liquid Film Flow in Spinning Cone Columns, Chemical Engineering Science, 53 (8), 1541-1550.

Makarytchev, S. V., T.A.G. Langrish and R. G. H. Prince, 2001, Thickness and Velocity of Wavy Liquid Films on Rotating Conical Surfaces, Chemical Engineering Science, 56, 77-87.

Makarytchev, S. V., T.A.G. Langrish and D. F. Fletcher, 2004, Mass Transfer Analysis of Spinning Cone Columns Using CFD, Chemical Engineering Research and Design, 82 (A6), 752-761.

Maruyama, T. and T. Maeuchi, 2008, Centrifugal-Force Driven Flow in Cylindrical Micro-Channel", Chemical Engineering Science 63, 153-156.

Miyazaki, H., 1971, Combined Free and Forced Convective Heat Transfer and Fluid Flow in a Rotating Curved Circular Tube, International Journal of Heat and Mass Transfer, 14, 1295-1309.

Mori, Y. and W. Nakayama, 1968, Convective Heat Transfer in Rotating Radial Circular Pipes, International Journal of Heat and Mass Transfer, 11, 1027-1040.

Ortiz-Osorio, J., J. M. MacInnes, P. J. Jordan, G. H. Priestman and R. W. K. Allen, Computation of Mass Transfer for Rotating Spiral Microchannel Distillation, 8th World Congress of Chemical Engineering, Montreal, July 2009.

Podbielniak, W. J., 1935, Centrifugal Fractionation Method and Apparatus, U. S. Patent 2,003,308.

Podbielniak, W. J., 1936, Method of Securing Counter Current Contact of Fluids by Centrifugal Action, U. S. Patent 2,044,996.

Podbielniak, W. J., 1937, Method and Apparatus of Refining Hydrocarbon Oil, U. S. Patent 2,093,645.

Podbielniak, W. J., ~~1937~~1938, Apparatus for Effecting Counter Current Contact Between Fluids, U. S. Patent 2,109,375.

Podbielniak, W. J., H. R. Kaiser and G. J. Ziegenhorn, 1970, Centrifugal Solvent Extraction, in The History of Penicillin Production, A. L. Elder, Editor, Chem. Eng. Prog. Symp. Series, No. 100, 46, New York: American Institute of Chemical Engineers.

Ramshaw, C. and R. H. Mallinson, 1981, Mass Transfer Process, U. S. Patent 4,283,255.

Rao, D. P., A. Bhowal and P. S. Boswami, 2004, Process Intensification in Rotating Packed Beds (Higee): An Appraisal, Ind. Eng. Chem. Res., 43, 1150-1162.

Salas, S. L. and E. Hille, Calculus, Second Edition, Xerox College Publishing, 1974.

Sherwood, T. K., R. L. Pigford and C. R. Wilke, Mass Transfer, McGraw-Hill, 1975.

Strand, C.P., R. B. Olney and G. H. Ackerman, 1962, Fundamental Aspects of Rotating Disk Contactor Performance, AIChE Journal, 8 (2), 252-261.

Tilley, B. S., S.H. Davis and S. G. Bankoff, 1994, Linear Stability Theory of Two-Layer Fluid Flow in an Inclined Channel, Physics of Fluids, 6 (12), 3906-3922.

Todd, D. B. and W. J. Podbielniak, 1965, Advances in Centrifugal Extraction, Chemical Engineering Progress, 61 (5), 69-73.

Visscher, F., J. van der Schaaf, T. A. Nijhuis and J. C. Schouten, 2013, Rotating Reactors – A Review, Chemical Engineering Research and Design, 91, 1923-1940.

Vivian, J. E., P. L. T. Brian and V. J. Krukonis, 1965, The Influence of Gravitational Force on Gas Absorption in a Packed Column, A.I.Ch.E. Journal, 11 (6), 1088-1091.

Wood, R. M. and B. E. Watts, 1973, The Flow, Heat and Mass Transfer Characteristics of Liquid Films on Rotating Discs, Transactions of the Institution of Chemical Engineers, 51, 315-322.

Zhao, H., Shao, L. & Chen, J.-F., 2010, High-Gravity Process Intensification Technology and Application, Chemical Engineering Journal, 156, 588-593.

Appendix

A.1 Temperature and pressure in the spiral

Knowledge of density and viscosity in each phase in the spiral flow is necessary to predict layer thickness using the wide-channel model. The following describes the method used to estimate temperature and pressure in the spiral channel so these properties can be determined.

A.1.1 Spiral Temperature

A single temperature for both phases and at each position along the channel is assumed. This single temperature is determined by measurement of the transient temperature at the glass exterior surface starting immediately after operation at a given rotation rate. When the rotating unit has come to rest, a thermocouple is sandwiched between foam insulation and the glass with the other side of the glass in contact with the PEEK element, so that during the measurement both sides of the glass lose little heat (the flows in the spiral are stopped). Heat transfer within the glass is approximated as one-dimensional and by fitting a suitable transient function to the recorded data the initial and final temperatures (T_o and T_f, respectively) of the exterior glass surface (in the absence of heat transfer with the overall device as it cools down). With these temperatures and the fact that the final temperature is the same as the initial mid-thickness value in the glass, the temperature at the interior glass surface during operation can be found. Taking this as representative of the temperature (T_S) in the spiral channel during operation:

$$T_S = T_o + 2(T_f - T_o) \qquad \text{A1.1}$$

The transient at the measured surface of the glass may be separated into the part associated with the one-dimensional heat transfer within the glass, having characteristic time δ^2/α = 125 s (δ = 1 cm and α = 8×10^{-7} m^2/s are the glass thickness and thermal diffusivity respectively), and the slower processes of lateral heat transfer in the glass and heat transfer with the overall device. The function suggested in Kuvshinov et al. (2010) for a similar application is effective here:

$$T(t) - T_0 = (T_f - T_o)\left(1 - \exp\left\{-\frac{t - t_0}{\tau}\right\}\right) + \gamma(t - t_0) \qquad \text{A1.2}$$

The first term represents the one-dimensional adjustment in the glass, while the second term is a linearisation of exponential terms with longer time scales. A typical fit to the transient data is shown in Fig. A1. The temperatures in this case are T_o = 34.8 °C and T_f = 36.5 °C giving an estimated spiral temperature of 38.2 °C. (The time constant of τ = 21.6 s in the fitted function is consistent with the characteristic time scale indicated above, as the time constant is typically around 20% of the characteristic time scale, e.g. MacInnes et al., 2005.)

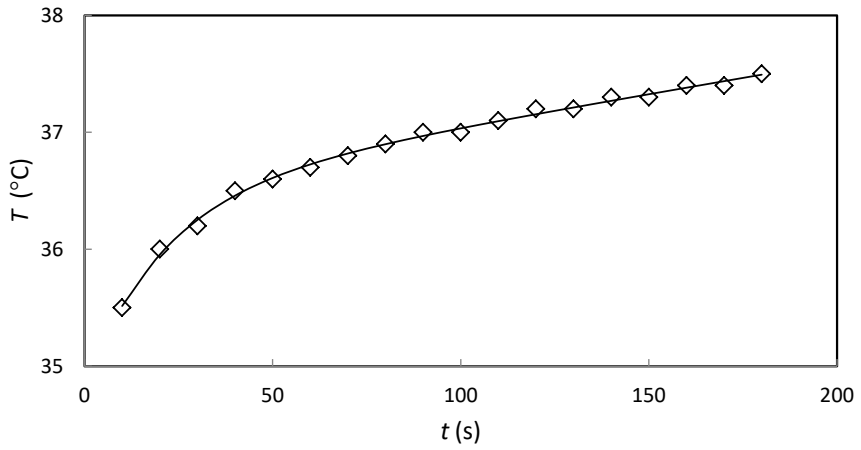

Figure A1. Transient of glass surface temperature immediately after stopping rotation and the fitted function given by Eq. A1.2 (data for 3840 rpm).

As may be expected, the spiral temperature was found to vary primarily with rotation rate, which determines both the bearing and seal friction heat generation rates. Data taken for a range of rotation rates and flow rates is shown in Fig. A2. The solid line is a power law function fit to the data and this is used to supply spiral temperature (in °C) for property determinations in the wide-channel model calculations:

$$T_S = 11.7\left(\Omega_{rpm} - 331\right)^{0.15} \qquad \text{A1.3}$$

This function fits the data with an rms deviation of 1.8 °C. Even the maximum deviations in the data correspond to changes in liquid viscosity giving just 4% change in liquid layer thickness in the wide channel model calculation.

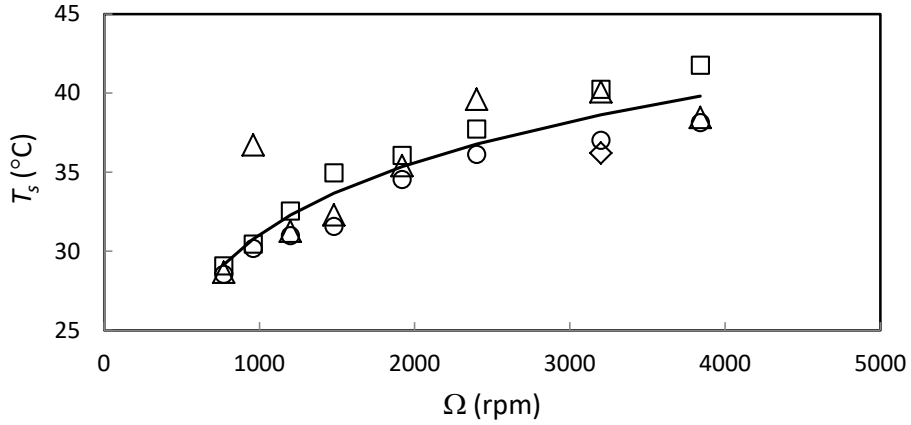

Figure A2. Correlation of spiral temperature and rotation rate.

A.1.2 Spiral Pressure

Pressure drop over the length of the spiral is small compared to absolute pressure for gas-liquid contacting. Thus, the pressure in the spiral can be taken as constant for purposes of gas property determination. The liquid outlet passage is sized so frictional losses are small compared to centrifugal hydrostatic pressure change and this allows the liquid outlet passage to serve as a manometer (Todd and Podbielniak, 1965). The spiral pressure then is given in terms of measured downstream liquid pressure (P_F , at point F in Fig. 2), the liquid density (ρ_L), the elevation difference between point F and the liquid level in the spiral reservoir (Δz) and the radial distances from the axis of rotation to the liquid level in the spiral reservoir and to the shaft surface at which the rotating part of the liquid passage ends (r_R and r_S , respectively). While passage frictional losses are neglected, the frictional loss in the flow exiting from the shaft hole into the seal passage is significant and is included, i.e. $\rho_L \Omega^2 r_S^2 / 2$, giving for the spiral pressure:

$$P_S = P_F + \frac{\rho_L \Omega^2}{2} r_R^2 - \rho_L g \Delta z \qquad \text{A1.4}$$

This result follows from the general relation (MacInnes et al., 2010, Maruyama and Maeuchi, 2008) between pressure, elevation differences, radial position differences and frictional losses in the flow between two sections in a rotating passage.